Journal of Sound and Vibration (2000) **229**(3), 627–645
doi:10.1006/jsvi.1999.2513, available online at http://www.idealibrary.com on IDEAL®

TRANSIENT TORSIONAL AND LATERAL VIBRATIONS OF UNBALANCED ROTORS WITH ROTOR-TO-STATOR RUBBING

B. O. AL-BEDOOR

Mechanical Engineering Department, King Fahd University of Petroleum & Minerals, KFUPM Box 841, *Dhahran* 31261, *Saudi Arabia*

(*Received* 9 *April* 1999, *and in final form* 4 *August* 1999)

This paper presents a model for the coupled torsional and lateral vibrations of unbalanced rotors that accounts for the rotor-to-stator rubbing. The system degrees of freedom, obtained using Lagrangian dynamics, are the rotor rigid-body rotation, the rotor torsional deformation and two orthogonal lateral deflections of the rotor. The rubbing condition is modelled using the elastic impact-contact idealization, which consists of normal and tangential forces at the rotor-to-stator contact point. The model is solved using a predictive-corrective numerical integration algorithm. The system response orbits show clearly the rotor-to-stator impact contact in the start-up period. The inclusion of rotor torsional flexibility has introduced irregular rubbing orbits. Rotor response anisotropy is observed in the rubbing responses for both lateral and lateral-torsional models. Furthermore, a split in resonance is observed due to the rubbing condition when the rotor torsional flexibility is considered. Finally, numerical simulations for rotors with non-zero fluid-film bearing cross-coupling terms have mainly shown a reduction in the split in resonance due to rubbing effects.

1. INTRODUCTION

With the increasing trend towards increased efficiency by operating rotors at higher speeds with lighter and more flexible shafts and very small clearances between rotors and stators, the probability of rotor-to-stator rubbing has increased tremendously. Due to the fact that no rotor can be perfectly balanced, the rotor-to-stator contact is most expected in the start-up period, when the rotor passes through its critical speed. A mathematical model that describes the coupled torsional and lateral vibrations of a rotor under the effect of rotor-to-stator rubbing is highly desirable. This model enables simulating the start-up dynamics of rotors under the effect of external driving torque and rubbing conditions. This model is crucial for development, design, commissioning, operations and diagnostics purposes.

Beatty [1] highlighted the destructive instability of rotors due to excessive rubbing between rotating and stationary parts. He proposed a mathematical

0022-460X/00/030627 + 19 $35.00/0

rationale for rubbing identification. The model used the elastic impact-contact model with Fourier series expansion for the mathematically generated rotor response signal with rubbing condition. Experimental data from industrial problems and controlled test-rig were used for evaluating the analytical prediction. It was proved that the spectral analysis is a valuable tool for rubbing identification before failure due to rubbing instabilities occurs. Beaty [1] concluded that synchronous vibration monitoring is not enough for rubbing evaluation, where second and third harmonics of the synchronous frequency have appeared due to rubbing. The harmonic amplitudes can be distorted by the transmission through the housing. Furthermore, he distinguished between rubbing conditions and bearing dead-band responses. Ehrich [2] studied the observations of high order sub-harmonic responses, up to the ninth, of high-speed rotors in bearing clearances. He used a two-degree-of-freedom (d.o.f) Jefcott rotor with piecewise linear stiffness. His computed results were compared with Muszynska's [3] experimental results up to the fourth sub-harmonic response orbits, where excellent qualitative agreement was found. He concluded that there are certain conditions on the non-linearity and damping for the eighth and ninth sub-harmonics to appear. A comprehensive literature survey on various phenomena during rubbing was reported by Muszynska [4]. Choi and Naoh [5] identified a complex mode locking in the non-linear phenomenon of a horizontal Jefcott rotor with bearing clearances modelled as discontinuous non-linearity. They utilized the winding-number map to measure the ratio between the two frequencies involved in the whirling motion. They located boundaries of each locking zone using the Floquet theory for checking the stability of periodic solutions, where period doubling bifurcation leading to chaos has occurred. Goldman and Muszynska [6] developed a new model for rotor–stator occasional rubbing. They used the polar co-ordinates for the two-d.o.f. rotor in which they modelled the impact as variable stiffness with associated damping effects. Their numerical simulations were presented in the form of lateral vibrations time-base waves, orbits and bifurcation diagrams. The system has shown orderly harmonic, sub-harmonic and chaotic responses. Recently, Chu and Zhang [7] reported results of their study on the non-linear vibration characteristics of a rub-impact of Jefcott rotor. Their model is two-dimensional with Beatty's [1] impact-contact model. Chu and Zhang [7] used the Fourier series and the Floquet theory to study the stability and bifurcation, qualitatively. Numerical integration with orbit and Poincare map data representation was used to quantitatively study the system behavior. They found three kinds of routes to chaos and quasi-periodic motion. The numerical integration was carried out for about 20 time intervals per revolution to ensure the disappearance of transient effects. To this end, one recognizes that all previously cited investigations have modelled the lateral vibrations of a rotor under rubbing condition while it is running at constant rotating speed. These studies were, mainly, devoted to the existence of sub-harmonic responses, bifurcation and chaotic vibrations at different, but steady state, velocities. The start-up dynamics for rotor systems driven by motors through connections that usually allow torsional flexibility cannot be evaluated using the present rubbing models. This need has motivated the present investigation, which presents a dynamical model to simulate the coupled

torsional and lateral vibrations of unbalanced rotor during the start-up period under the effect of rubbing conditions.

The present work is devoted towards developing a mathematical model for the coupled torsional and lateral vibrations of unbalanced rotors under the effect of rotor-to-stator rubbing conditions in the start-up period. The model is developed using Lagrangian dynamics to account for the rotor torsional flexibility as an independent d.o.f. To accomplish this objective two successive transformations were employed. The system d.o.f.s are the rotor rigid-body rotation, the rotor torsional deformation angle and two-orthogonal lateral deflections of the rotor. The rubbing condition is modelled using the elastic impact-contact idealization which produces normal and tangential forces at the rotor-to-stator contact point. The normal and tangential forces are functions of the stator stiffness and the stator–rotor coefficient of sliding friction. To account for the effect of fluid-film bearing stiffness and damping cross-coupling terms, the lumped-parameter speed-dependent model, which was presented by Tam *et al.* [8], is adopted. The equations of motion are represented in a compact matrix and solved for different cases using a predictor–corrector integration scheme. The obtained results are discussed and a number of observations on the rotor system dynamic behavior are extracted.

2. THE DYNAMIC MODEL

2.1. SYSTEM DESCRIPTION AND ASSUMPTIONS

A schematic diagram of a disc–shaft system driven by electrical motor and supported by two fluid bearings is shown in Figure 1. The model is developed with the following assumptions: (1) the model adopts the simple Jeffcot approach that considers the system as a massive rigid disk mounted midway between the bearings on a massless flexible shaft, (2) the moving mass, M, is not only the mass of the disk but the modal mass that corresponds to the first lateral mode of the system, (3) the approach is valid below the second-lateral critical speed, (4) the lateral stiffness is

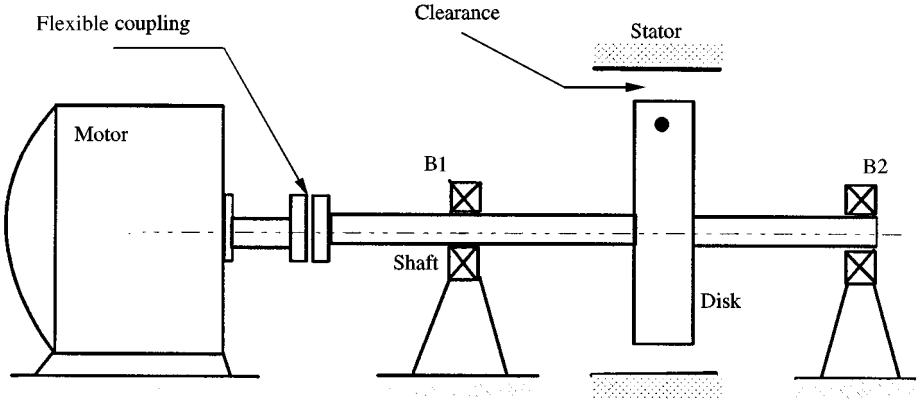

Figure 1. Schematic of the motor–shaft–disk and stator system.

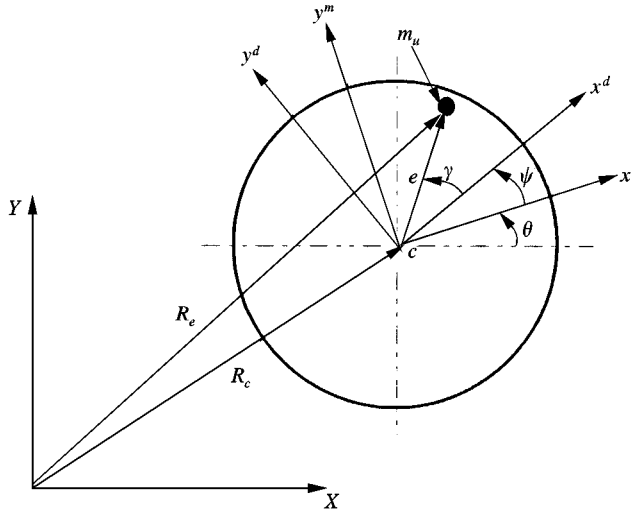

Figure 2. Co-ordinate systems and the deformed system configuration.

the shaft flexural stiffness which is assumed to be relatively small compared to the bearing stiffness, (5) the bearings have only linear viscous damping effects and (6) the gyroscopic effects due to disk spinning are neglected.

The system d.o.f.s are lumped at the disk as two orthogonal lateral deflections of the disk geometrical center (X, Y), one rigid-body rotation, θ and one torsional deflection angle, ψ. The co-ordinate systems used in developing the model are shown in Figure 2, wherein, XY is the inertial reference frame, $x^m y^m$ is a body co-ordinate system of the motor shaft which is rotating with the torsionally undeflected system, xy is a body co-ordinate system of the disk which is attached to the disk and exhibits all its motions. The mass imbalance, m_u, location is described by the eccentricity vector e with respect to the disk body co-ordinate system xy. The model is developed using Lagrangian dynamics in the inertial co-ordinate system.

2.2. KINETIC ENERGY EXPRESSIONS

The kinetic energy of the shaft disk system is constituted of the motor kinetic energy, the disk kinetic energy and the mass unbalance kinetic energy. The rotor system kinetic energy can be written as

$$U_D = \tfrac{1}{2}M(\dot{X}^2 + \dot{Y}^2) + \tfrac{1}{2}J_D(\dot{\theta} + \dot{\psi})^2 + \tfrac{1}{2}J_M\dot{\theta}^2 + \tfrac{1}{2}m_u\dot{\mathbf{R}}_e^{\mathrm{T}}\dot{\mathbf{R}}_e, \tag{1}$$

where J_M is the motor mass moment of inertia, M is the rotor modal mass, J_D is the disk mass moment of inertia, m_u is the unbalance mass and $\dot{\mathbf{R}}_e$ is the velocity vector of the unbalance mass in the inertial reference frame. According to the system deformed configuration, shown in Figure 2, the global position vector of the mass unbalance, can be written as

$$\mathbf{R}_e = [\mathbf{A}(\theta)][\mathbf{A}(\psi)]\mathbf{e}, \tag{2}$$

where **e** is the position vector of m_u in the disk body co-ordinate system xy, $[\mathbf{A}(\theta)]$ is the rotational transformation matrix from the motor co-ordinate system to the inertial reference frame, XY, and $[\mathbf{A}(\psi)]$ is the rotational transformation matrix from the disk co-ordinate system, xy, to the motor co-ordinate system. The rotational transformation matrices $[\mathbf{A}(\theta)]$ and $[\mathbf{A}(\psi)]$ can be represented, respectively, as

$$[\mathbf{A}(\theta)] = \begin{bmatrix} \cos\theta & -\sin\theta \\ \sin\theta & \cos\theta \end{bmatrix} \tag{3}$$

$$[\mathbf{A}(\psi)] = \begin{bmatrix} 1 & -\psi \\ \psi & 1 \end{bmatrix} \tag{4}$$

where θ represents the motor rigid-body rotation and ψ represents the torsional deformation angle measured with respect to the motor co-ordinate system. The transformation matrix $[\mathbf{A}(\psi)]$ is linearized based on the assumption of small torsional deformations.

The velocity vector of the mass imbalance in the inertial reference frame can be obtained by differentiating equation (2) as follows:

$$\dot{\mathbf{R}}_e = \dot{\theta}[\mathbf{A}_\theta(\theta)][\mathbf{A}(\psi)]\mathbf{e} + \dot{\psi}[\mathbf{A}(\theta)][\mathbf{A}_\psi(\psi)]\mathbf{e} \tag{5}$$

where $[\mathbf{A}_\theta]$ and $[\mathbf{A}_\psi]$ represent the derivatives $[\mathrm{d}\mathbf{A}(\theta)/\mathrm{d}\theta]$ and $[\mathrm{d}\mathbf{A}(\psi)/\mathrm{d}\psi]$, respectively.

Upon substituting for $[\mathbf{A}_\theta]$ and $[\mathbf{A}_\psi]$ into equation (5), the velocity vector of the mass imbalance, m_u, in the inertial reference frame can be represented in the form

$$\dot{\mathbf{R}}_e = \begin{Bmatrix} \dot{X} - \dot{\theta}e_x\alpha - \dot{\theta}e_y\beta - \eta\dot{\psi} \\ \dot{Y} + \dot{\theta}e_x\beta - \dot{\theta}e_y\alpha + \mu\dot{\psi} \end{Bmatrix}, \tag{6}$$

where

$$\begin{aligned} &\alpha = \sin\theta + \psi\cos\theta,\ \beta = \cos\theta - \psi\sin\theta, \\ &\eta = e_x\sin\theta + e_y\cos\theta,\ \mu = e_x\cos\theta - e_y\sin\theta. \end{aligned} \tag{7}$$

Substituting equation (6) into equation (1), the rotor system kinetic energy becomes

$$\begin{aligned} U = {} & \tfrac{1}{2}(m_u + M)(\dot{X}^2 + \dot{Y}^2) + \tfrac{1}{2}m_u e^2\dot{\theta}^2(1 + \psi^2) + \tfrac{1}{2}m_u e^2\dot{\psi}^2 \\ & - m_u\dot{X}\dot{\theta}[(e_x - \psi e_y)\sin\theta + (e_x\psi + e_y)\cos\theta] \\ & + m_u\dot{Y}\dot{\theta}[(e_x - \psi e_y)\cos\theta - (e_x\psi + e_y)\sin\theta] \\ & - m_u\dot{X}\dot{\psi}(e_x\sin\theta + e_y\cos\theta) + m_u\dot{Y}\dot{\psi}(e_x\cos\theta - e_y\sin\theta) \\ & + m_u e^2\dot{\theta}\dot{\psi} + \tfrac{1}{2}J_M\dot{\theta}^2 + \tfrac{1}{2}J_D(\dot{\theta} + \dot{\psi})^2. \end{aligned} \tag{8}$$

2.3. POTENTIAL ENERGY EXPRESSIONS

The system potential energy consists of the shaft bending strain energy and the torsional strain energy. The elastic strain energy of the shaft is given by

$$V = \tfrac{1}{2}k_X X^2 + \tfrac{1}{2}k_Y Y^2 + \tfrac{1}{2}k_T\psi^2. \tag{9}$$

2.4. THE EQUATIONS OF MOTION

Upon substituting the kinetic and potential energy expressions into the Lagrange's equation, performing the needed differentiation and manipulation, the system equation of motion is found as

$$\begin{bmatrix} m_{\theta\theta} & m_{\theta\psi} & m_{\theta X} & m_{\theta Y} \\ m_{\psi\theta} & m_{\psi\psi} & m_{\psi X} & m_{\psi Y} \\ m_{X\theta} & m_{X\psi} & m_{XX} & 0 \\ m_{Y\theta} & m_{Y\psi} & 0 & m_{YY} \end{bmatrix} \begin{Bmatrix} \ddot{\theta} \\ \ddot{\psi} \\ \ddot{X} \\ \ddot{Y} \end{Bmatrix} + \begin{bmatrix} 0 & 0 & 0 & 0 \\ 0 & C_{\psi\psi} & 0 & 0 \\ 0 & 0 & C_{XX} & C_{XY} \\ 0 & 0 & C_{YX} & C_{YY} \end{bmatrix} \begin{Bmatrix} \dot{\theta} \\ \dot{\psi} \\ \dot{X} \\ \dot{Y} \end{Bmatrix}$$

$$+ \begin{bmatrix} 0 & 0 & 0 & 0 \\ 0 & k_{\psi\psi} & 0 & 0 \\ 0 & 0 & k_{XX} & k_{XY} \\ 0 & 0 & k_{YX} & k_{YY} \end{bmatrix} \begin{Bmatrix} \theta \\ \psi \\ X \\ Y \end{Bmatrix} + \begin{Bmatrix} Q_\theta \\ 0 \\ Q_X \\ Q_Y \end{Bmatrix} = \begin{Bmatrix} F_\theta \\ F_\psi \\ F_X \\ F_Y \end{Bmatrix}, \tag{10}$$

where

$$m_{\theta\theta} = J_M + J_D + m_u e^2(1 + \psi^2), \tag{11}$$

$$m_{\theta\psi} = m_{\psi\theta} = m_{\psi\psi} = J_D + m_u e^2, \tag{12}$$

$$m_{\theta X} = m_{X\theta} = -\, m_u \lfloor (e_x - \psi e_y)\sin\theta + (e_x\psi + e_y)\cos\theta \rfloor, \tag{13}$$

$$m_{\theta Y} = m_{Y\theta} = m_u \lfloor (e_x - \psi e_y)\cos\theta - (e_x\psi + e_y)\sin\theta \rfloor, \tag{14}$$

$$m_{\psi X} = m_{X\psi} = -\, m_u \lfloor e_x \sin\theta + e_y \cos\theta \rfloor, \tag{15}$$

$$m_{\psi Y} = m_{Y\psi} = m_u \lfloor e_x \cos\theta - e_y \sin\theta \rfloor, \tag{16}$$

$$m_{XX} = m_{YY} = M + m_u, \tag{17}$$

$$k_{\psi\psi} = k_T - m_u e^2 \dot{\theta}^2, \tag{18}$$

$$Q_\theta = 2m_u e^2 \psi \dot{\psi} \dot{\theta}, \tag{19}$$

$$Q_X = 2m_u \dot{\theta}\dot{\psi}(e_y \sin\theta - e_x \cos\theta) - m_u \dot{\theta}^2 [(e_x - \psi e_y)\cos\theta - (e_x\psi + e_y)\sin\theta], \tag{20}$$

$$Q_Y = -\, 2m_u \dot{\theta}\dot{\psi}(e_x \sin\theta + e_y \cos\theta) - m_u \dot{\theta}^2 [(e_x - \psi e_y)\sin\theta + (e_x\psi + e_y)\cos\theta], \tag{21}$$

The first matrix in equation (10) is the system inertia matrix which shows coupling between the system d.o.f. Equation (11) shows the angular motion, θ, mass moment of inertia. It is shown that this inertia is affected by the imbalance and non-linearly affected by the torsional d.o.f., ψ. The torsional d.o.f. mass moment of inertia and the inertia coupling between the θ and ψ d.o.f.s are shown in equation (12) and are affected by the imbalance inertia. Equations (13) and (14) show that the

coupling between the rotor lateral d.o.f. X, Y and the system reference rotational motion, θ, is function of the imbalance and torsional deformation angle and these are periodic functions. The inertia couplings between the system lateral motions and the torsional deformation are, shown in equations (15, 16), functions of the imbalance and they are periodic functions of θ. Finally, the mass corresponding to the lateral motions of the system is shown in equation (17) with no inertia coupling between them.

The second and third matrices represent the damping and stiffness matrices of the system. One point that is interesting and appears for the first time in this study, is the softening effect that the system rotation has on the system torsional stiffness $k_{\psi\psi}$ as shown in equation (18). It is worth mentioning that this term could not be obtained following the traditional approach of having the torsional d.o.f. as small motion superimposed on the system rotational motion. The fourth term in equation (10) is the non-linear vector associated with each d.o.f. The non-linear part corresponding to the θ d.o.f. is given in equation (19) and shown to be function of the system rotational speed, the torsional deformation angle and its time derivative and the mass imbalance. The non-linear terms corresponding to the system lateral d.o.f.s, X and Y are given by equations (20) and (21) respectively. The first term in equations (20) and (21) occurs as a result of torsional deformation and the second term is the known effect of imbalance, which is now function of the torsional deformation angle. To this end, one recognizes that the adopted approach that deals with the torsional deformation angle as an individual d.o.f. has resulted in terms that were not shown in previous models. In particular, the inertia coupling terms, the softening effect of the torsional stiffness and some of the non-linear terms as denoted by Q_θ, Q_X and Q_Y. The right-hand side vector is the vector of external forces and torque. The first entry is the motor torque which is responsible for feeding the rotational motion into the system. The other three entries take care of external applied radial forces and torque as well as, in this study, of the impulsive forces and torque developed as a result of rotor-to-stator rubbing.

3. RUBBING FORCES

The rotor and stator cross-sections are assumed to be circular and the rubbing-impact occurs occasionally with very short duration of time. The elastic impact assumption is adopted, based on the consideration of hard surfaces for rotor and stator [6], with no associated damping effects. It should not be understood that the conventional coefficient of restitution is taken to be one in this model. The model utilizes the discontinuous spring approach which was proved [1, 2], to be working correctly for similar problems. The adopted model produces two forces during the contact period as shown in Figure 3(a). The forces are the normal and the frictional forces which can be expressed, respectively, as follows [1]:

$$F_N = \begin{cases} k_s(R - \Delta), & (\text{for } R \geqslant \Delta), \\ 0, & (\text{for } R < \Delta), \end{cases} \tag{22}$$

$$F_T = \mu F_N,$$

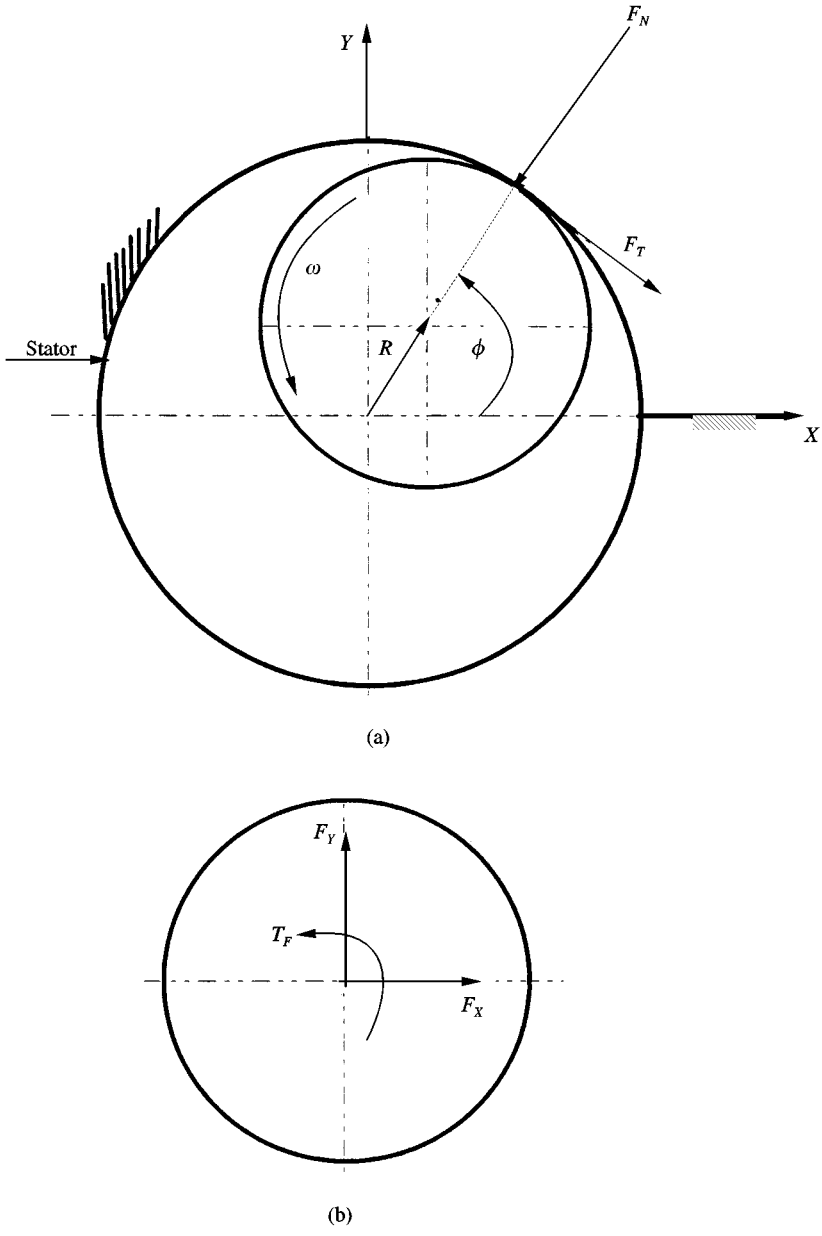

Figure 3. (a) Schematic of the rubbing-impact forces. (b) Schematic of the rotor geometrical center forces and torque.

where k_s is the stator radial stiffness which is usually higher than the shaft radial stiffness, Δ is the radial clearance between the rotor and the stator, μ is the sliding friction coefficient and R is the radial response of the rotor geometrical center which can be expressed as

$$R = \sqrt{X^2 + Y^2}, \quad \text{where } \cos\phi = \frac{X}{Y} \text{ and } \sin\phi = \frac{Y}{R}. \tag{23}$$

For a rotor disk with radius R_D, making use of equation (23), the normal and frictional forces can be transformed to the rotor geometrical center, as shown in Figure 3(b), to give two forces and one couple as follows respectively

$$\begin{Bmatrix} F_X \\ F_Y \end{Bmatrix} = \frac{k_s(R-\Delta)}{R} \begin{bmatrix} -1 & \mu \\ -\mu & -1 \end{bmatrix} \begin{Bmatrix} X \\ Y \end{Bmatrix} \quad \text{for } R \geqslant \Delta. \tag{24}$$

$$T_F = -R_D \mu k_s (R-\Delta)$$

4. NUMERICAL SIMULATION AND DISCUSSION

The model of equation (10) is solved using a predictive–corrective time integration algorithm. The base data of the shaft–disk system, as taken from Lallane and Ferraris [9], are shown in Table 1. The stator stiffness $k_s = 5 \times 10^8$ N/m and the coefficient of sliding friction between the rotor and stator is taken as $\mu = 0{\cdot}2$. The system is solved and the data is recorded at a very short time step, $\Delta t = 0{\cdot}001$ s, to make sure that small changes in the system response due to impact-contact condition are captured. Using the inverse dynamic procedure, the motor torque is designed to rotate the rotor system to an angular velocity of 10 000 r.p.m. in 20 s. The torque profile and the resulting rotor velocity curve are shown in Figure 4(a) and 4(b) respectively. The numerical study constitutes three parts. One part is the simulation of the rotor response during the start-up period, with and without rubbing conditions, using the lateral-rotor model, i.e., no torsional flexibilities accounted for.

The second part is the simulation of the rotor response using the torsional–lateral-rotor model. In the first and second parts, the bearing is modelled with zero cross-coupling stiffness and damping coefficients, $C_{XY} = C_{YX} = k_{XY} = k_{YX} = 0$, to shed more light on the rubbing effects. Part three of the numerical simulation

TABLE 1

Disk–Shaft Data

Property	Value
Disk inner and outer radius	0·01, 0·15 m
Disk thickness	0·03 m
Disk mass M	16·47 kg
Disk moment of inertia, J_D	0·1861 kg m^2
Motor moment of inertia, J_M	0·36 kg m^2
Shaft stiffness k_{XX}, k_{YY}	5×10^5 N/m
Imbalance mass m_u	10^{-4} kg
Imbalance eccentricity e	0·15 m
Lateral modes damping ratio ζ_l	0·0175
Torsional mode damping ratio ζ_T	$1{\cdot}23 \times 10^{-3}$
Stator stiffness coefficient, k_s	5×10^8 N/m
Stator–rotor friction coefficient, μ	0·2

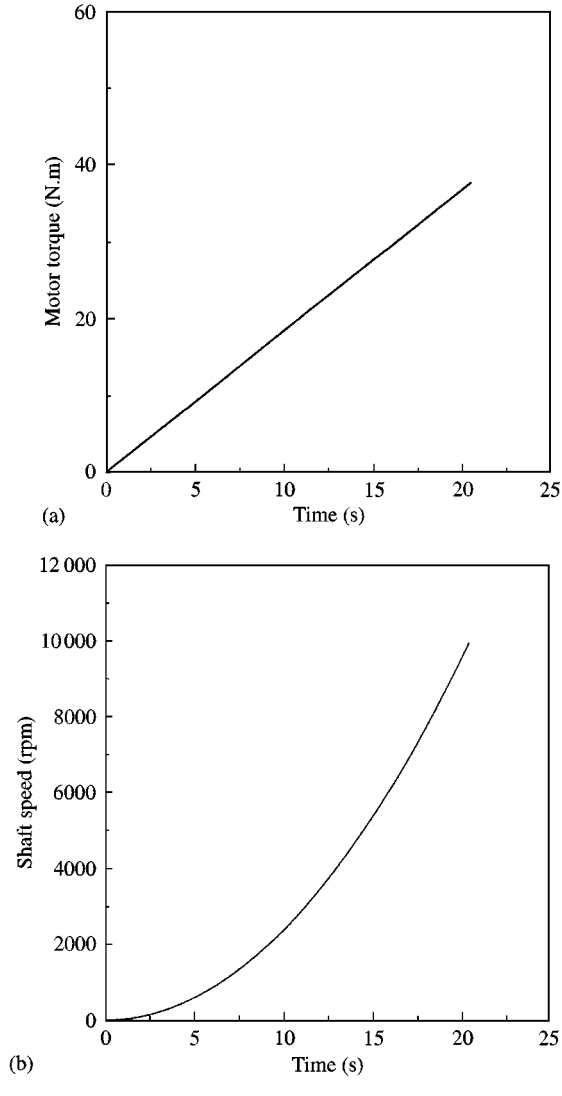

Figure 4. (a) Motor torque to rotate the system to a speed of 10 000 r.p.m. (b) Rotor angular velocity.

presents the rotor-system lateral and torsional vibration responses when the non-zero bearing cross coupling stiffness and damping terms are considered. The results of the three parts are presented and discussed in the following subsections, respectively.

4.1. THE LATERAL ROTOR MODEL

The dynamic model given by equation (10) is reduced to account only for the rotor lateral deflections, X, Y and rigid-body rotation θ, where the torsional d.o.f. is eliminated. The torque profile shown in Figure 4(a) is applied and the rotor

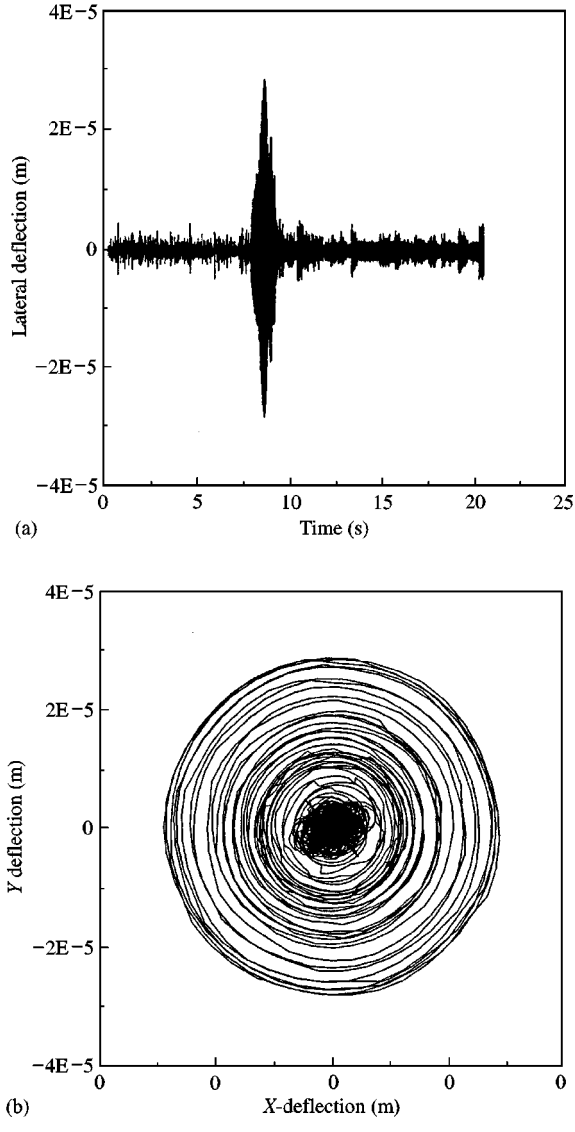

Figure 5. Rotor system response using the lateral-rotor model without torsional flexibility and no rubbing: (a) vertical deflection, and (b) orbit.

response is shown in Figure 5(a) and (b) for the vertical deflection and the orbit respectively. Figure 5(a) shows the occurrence of resonance at the rotor critical speed, $\dot{\theta} = 1663{\cdot}8$ r.p.m. The orbit shown in Figure 5(b) is circular as a result of rotor isotropy. The circle starts to grow until it reaches the maximum R at resonance, then goes back in a regular fashion. The maximum response vector amplitude is found to be $R = 2{\cdot}88 \times 10^{-5}$ m.

In order to simulate a case where rubbing is involved, a clearance $\Delta = 2{\cdot}65 \times 10^{-5}$ m is allowed. This means that the maximum response vector R is greater than the allowable clearance between the rotor and the stator and rubbing

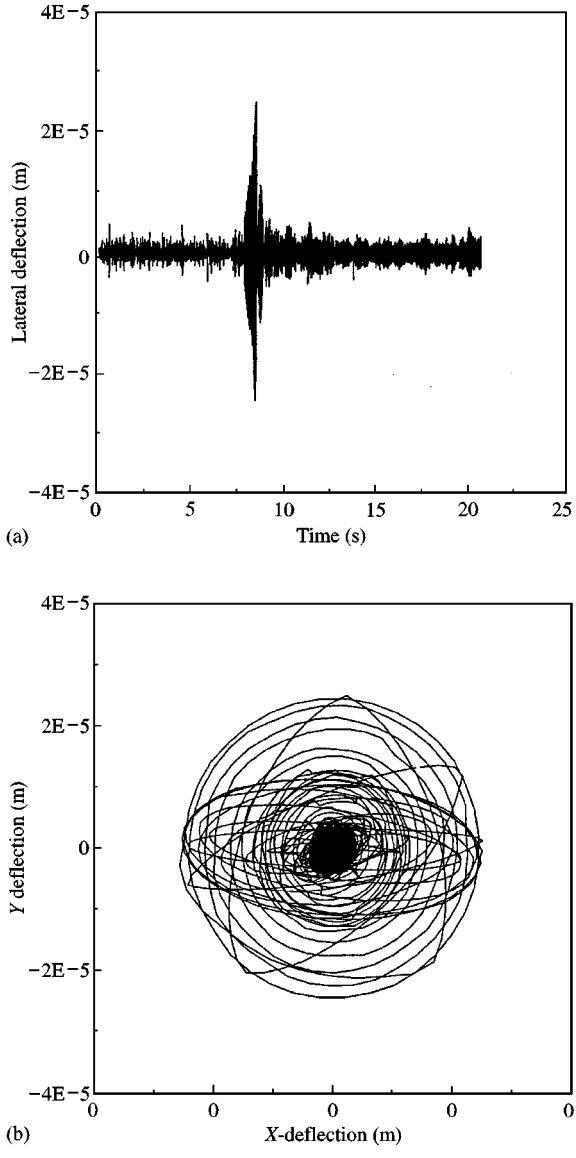

Figure 6. Rotor system response using the lateral-rotor model without torsional flexibility and with rotor-to-stator rubbing: (a) vertical deflection, and (b) orbit.

will occur. The torque of Figure 4(a) is applied and the system response is shown in Figure 6. The time history of the rotor vertical deflection, Figure 6(a), shows that the deflection is limited by the allowable clearance. Figure 6(b) shows the rotor orbit response where the rotor rebounds from the stator to impact it again until it enters a very regular elliptical orbit that touches the stator along a line that is parallel to the x-axis. This behavior can be attributed to the stiffness anisotropy introduced by the asymmetry of the induced frictional forces, equation (24). It is worth mentioning that the selection of the clearance should be done with care, as

unrealistic penetration of the rotor into the stator wall cannot be simulated using the proposed model. Detailed penetration-impact model that takes into account the local non-linear and plastic deformations is needed.

4.2. THE LATERAL-TORSIONAL ROTOR MODEL

The dynamic model of equation (10) is now simulated in full, where the d.o.f.s are the rigid-body rotation θ, the rotor torsional deformation angle ψ and the rotor two lateral deflections X and Y. The data are shown in Table 1, except the torsional stiffness coefficient, k_T, which is left to decide the relation between the rotor torsional and lateral natural frequencies. This relation should be selected carefully as reported by A1-Bedoor [10]. For example, the rotor response is simulated when the torsional and lateral natural frequencies are equal, $\omega_T = \omega_L$. The rotor system response is shown in Figure 7. Figure 7(a) shows the lateral deflection, in which there are two resonance points. One resonance is the ordinary one and the second is the one that developed as a result of the parametric excitation coupling between

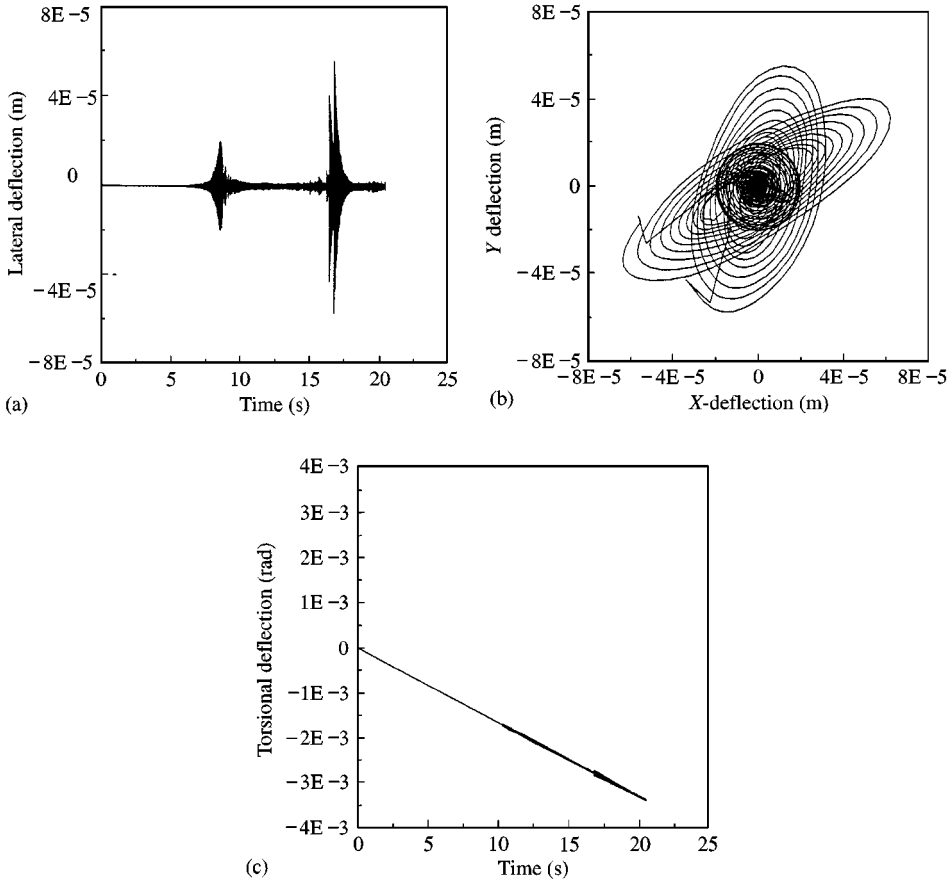

Figure 7. Rotor system response using the lateral–torsional-rotor model, $\omega_T = \omega_L$ without rotor-to-stator rubbing: (a) vertical deflection, (b) orbit and (c) torsional deflection.

the torsional and lateral rotor modes. An interesting behavior is shown in the orbit, Figure 7(b), which shows that the direction of the two maximum responses changes.

Furthermore, an anisotropy in the rotor response is shown in the orbit as a result of the torsional–lateral vibration interaction. Figure 7(c) shows the torsional deformation of the rotor where quasi-static deflection is noticed with very small oscillations superimposed at its end. The quasi-static deflection is expected as a result of the torsional inertia torque due to rotor angular acceleration.

To avoid having the rotor torsional–lateral parametric interaction superimposed on the rotor–stator rubbing effect, the rotor is simulated with relatively high torsional stiffness, $k_T = 25\,\mathrm{kN\,m/rad}$, that gives $\omega_T \gg \omega_L$. The rotor system response is shown in Figure 8, in terms of lateral deflection time history, orbit and torsional deformation time history. Figure 8(a) shows the rotor vertical deflection which indicates that the maximum deflection at resonance is reduced by including the torsional flexibility into the model. The orbit, Figure 8(b), shows smoother response than that of the lateral model. The maximum response at resonance is found, from Figure 8(b), $R = 1{\cdot}88 \times 10^{-5}\,\mathrm{m}$.

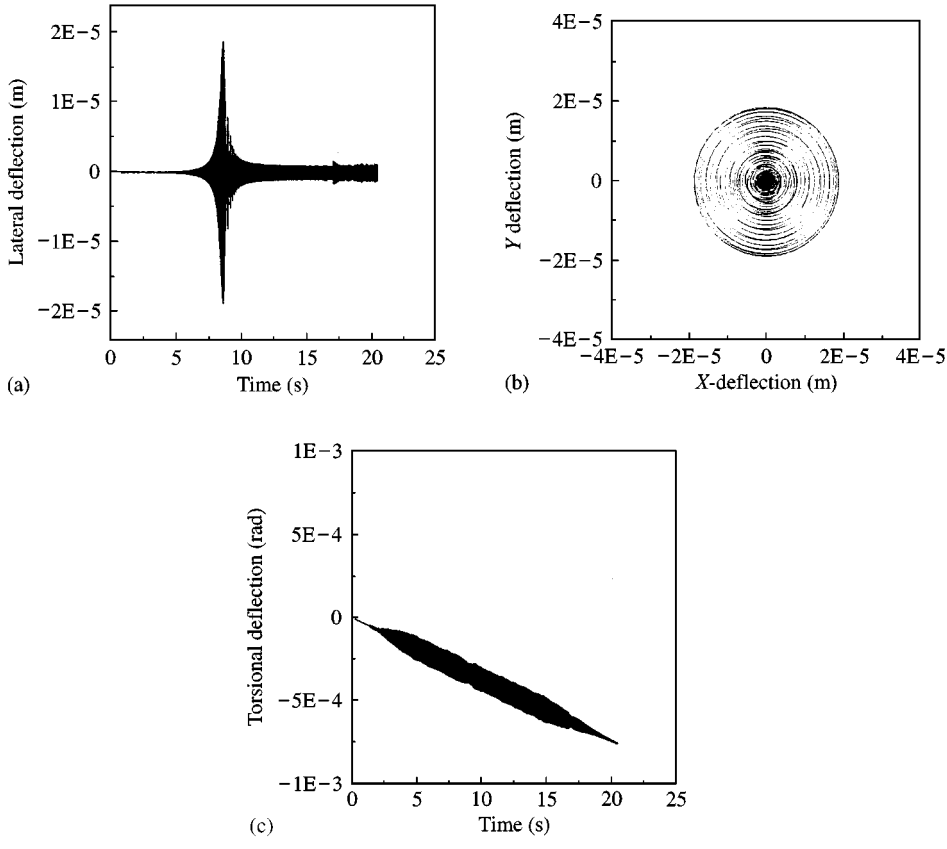

Figure 8. Rotor system response using the lateral–torsional-rotor model, $\omega_T \gg \omega_L$, with rotor-to-stator rubbing: (a) vertical deflection, (b) orbit and (c) torsional deflection.

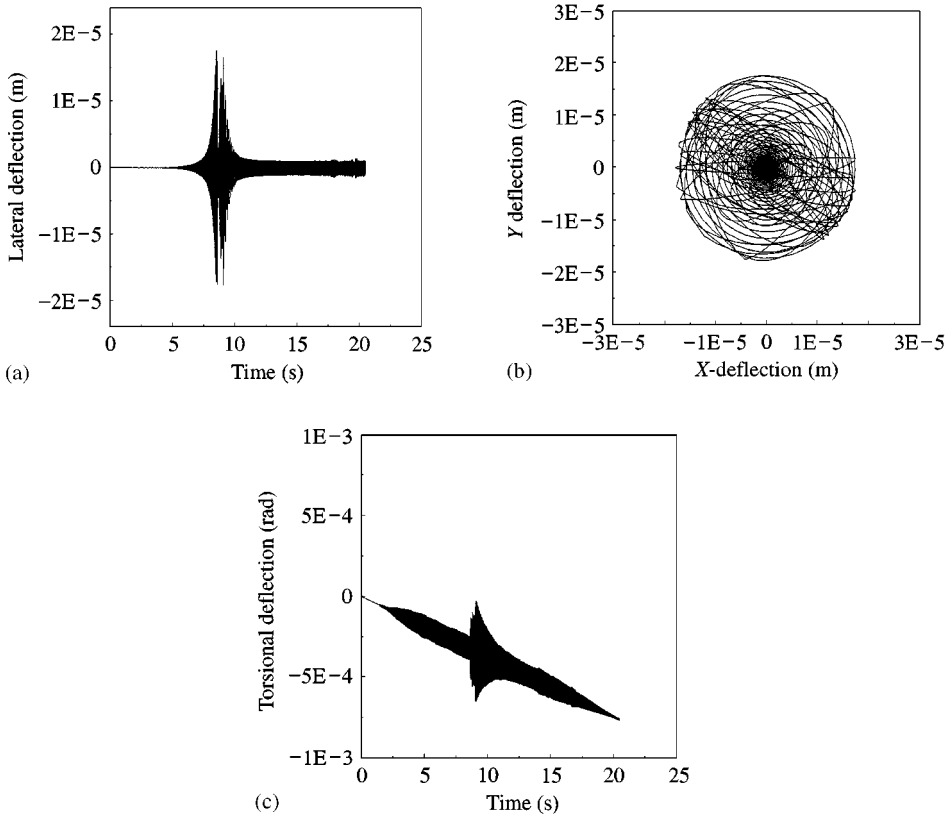

Figure 9. Rotor system response using the lateral–torsional-rotor model, $\omega_T \gg \omega_L$, with rotor-to-stator rubbing: (a) vertical deflection, (b) orbit and (c) torsional deflection.

To simulate rubbing occurrence, a clearance $\Delta = 1{\cdot}7 \times 10^{-5}$ m is used in the program and the rotor response is shown in Figure 9. The rotor vertical deflection is shown in Figure 9(a), where a split at resonance has occurred as a result of impact-contact between the rotor and the stator. Figure 9(b) shows the resulting orbit where many contacts between the rotor and the stator can be seen. The regularity of rotor motion within the stator clearance, which was observed in the lateral-rotor model simulation, Figure 6(b), is lost and the number of contacts has increased in irregular fashion. This kind of behavior may be given the name of chaotic vibrations and can be further investigated by using the Poincare maps or Liaponuv's exponents. This type of analysis needs the running of the rotor system at constant rotational velocities for long periods of time, i.e., steady state response, which is beyond the scope of the present transient start-up analysis. The rotor torsional deformation angle, Figure 9(c), shows that the torsional vibration is excited by the frictional torque at the contact instant, but damped stable oscillations.

4.3. BEARING CROSS-COUPLING EFFECTS

In order to simulate the rotor rubbing responses under the effect of fluid-film stiffness and damping cross-coupling effects, the lumped parameter bearing model

which was presented by Tam *et al.* [8] is adopted. The model utilizes the average circumferential fluid velocity, λ, and was proved to be powerful in representing bearing/seal fluid dynamic forces. Accordingly, the X and Y bearing fluid forces are represented [8] as

$$-F = \begin{bmatrix} K & D\lambda\Omega \\ -D\lambda\Omega & K \end{bmatrix} \begin{Bmatrix} X \\ Y \end{Bmatrix} + \begin{bmatrix} D & m_f\lambda\Omega \\ -2m_f\lambda\Omega & D \end{bmatrix} \begin{Bmatrix} \dot{X} \\ \dot{Y} \end{Bmatrix}, \tag{25}$$

where $K = k_{XX} = k_{YY}$, $D = C_{XX} = C_{YY}$ and the cross-coupling terms, shown in equation (10), are $k_{XY} = D\lambda\Omega$ and $C_{XY} = 2m_f\lambda\Omega$, where Ω is the changing rotor velocity. The values of the fluid average velocity λ and the fluid inertia m_f are taken as identified by Tam *et al.* [8] as 0·125 and 4·6 kg respectively.

The rotor system responses, under the effects of bearing cross-coupling terms and no rubbing condition, are shown in Figure 10. Figure 10(a), (b) and (c) show the rotor vertical deflection, the rotor orbit and the rotor torsional vibrations respectively. Upon comparing the rotor responses of Figure 10 with their corresponding ones in Figure 8, with zero bearing cross-coupling terms, only differences in the maximum lateral deflection amplitude can be noticed. Other qualitative behavior is the same with and without the inclusion of the bearing cross-coupling terms. Under the condition of rotor-to-stator rubbing, the rotor lateral and torsional vibrations are shown in Figure 11. Comparison of Figure 11(a) with Figure 9(a) (with zero bearing coupling terms) shows that the split in resonance to rubbing condition is minimized due to the effect of bearing cross-coupling stiffness and damping coefficients. Consequently, the number of rotor-to-stator contacts is reduced, in the orbit of Figure 11(b) if compared with Figure 9(b). The rotor torsional vibration response, Figure 11(c), shows no change when compared with Figure 9(c). However, it is hard to generalize on the combined effects of bearing cross-coupling terms and rubbing condition, as the problem is parameter dependent and further parametric analytical and experimental studies are recommended.

5. CONCLUSIONS

In this study, a model for the coupled torsional and lateral vibrations of unbalanced rotors that accounts for the rotor-to-stator rubbing is developed. The appropriate coupling between the unbalanced rotor torsional and lateral vibrations is achieved by utilizing two successive transformation matrices. The system d.o.f.s, obtained using the Lagrangian dynamics, are the rotor rigid-body rotation, the rotor torsional deformation and the rotor two orthogonal lateral deflections. The rubbing condition is modelled using the elastic impact-contact idealization, which consists of normal and tangential forces at the rotor-to-stator contact point. When transferred to the rotor geometrical center, the normal and tangential forces produced two forces and one couple. The effects of fluid-film bearing are accounted for by utilizing the lumped-parameter average circumferential fluid velocity model. The model is solved using a

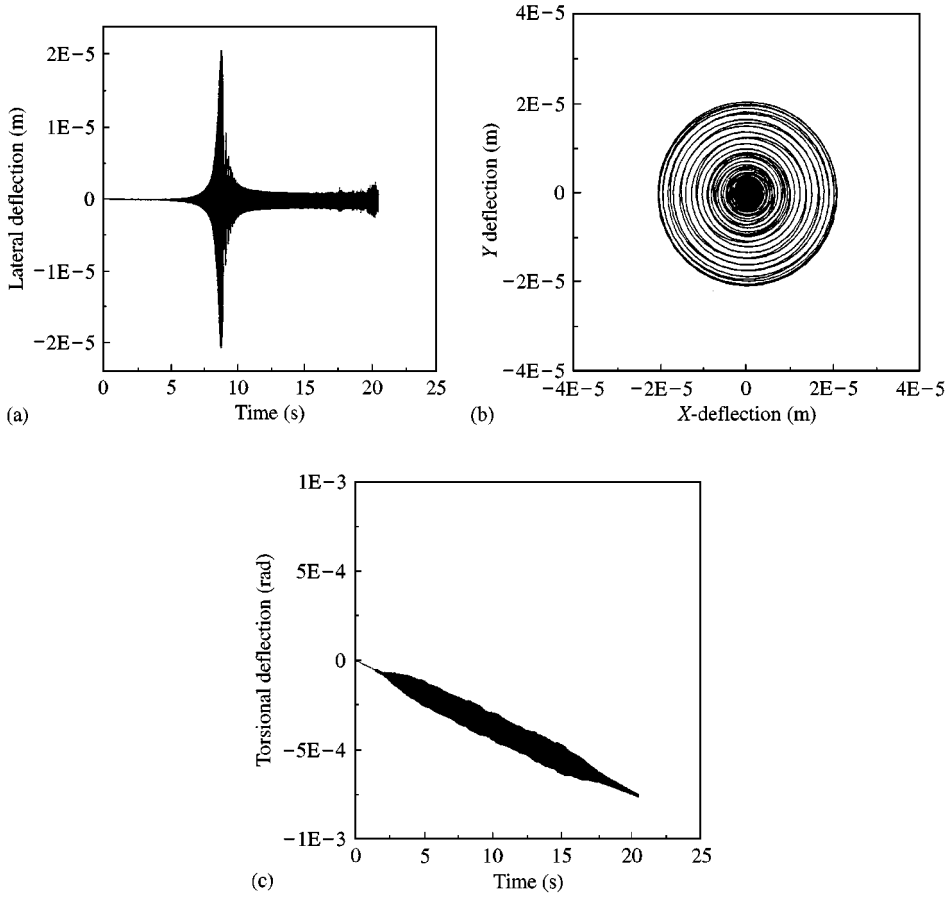

Figure 10. Rotor system response using the torsional–lateral-rotor model with $\omega_T \gg \omega_L$, non-zero cross-coupling bearing coefficients and no rubbing: (a) vertical deflection, (b) orbit, and (c) torsional deflection.

predictive–corrective numerical integration algorithm with very small time increments to assure capturing all changes in the dynamics due to impact-contact conditions. The system response orbits showed clearly the rotor-to-stator impact contact in the start-up period. The inclusion of rotor torsional flexibility has introduced irregular rubbing orbits when compared with the rubbing orbits obtained using the rotor lateral model. Rotor response anisotropy is observed in the rubbing responses for both lateral and lateral-torsional models. A split in resonance is observed due to the rubbing condition when the rotor torsional flexibility is considered. This split in resonance is reduced when the non-zero bearing cross-coupling coefficients are considered and consequently the number of rotor-to-stator contacts is reduced. Finally, the proposed approach of modelling the rotor rubbing response in the start-up period is recommended for adoption in larger-scale rotor models.

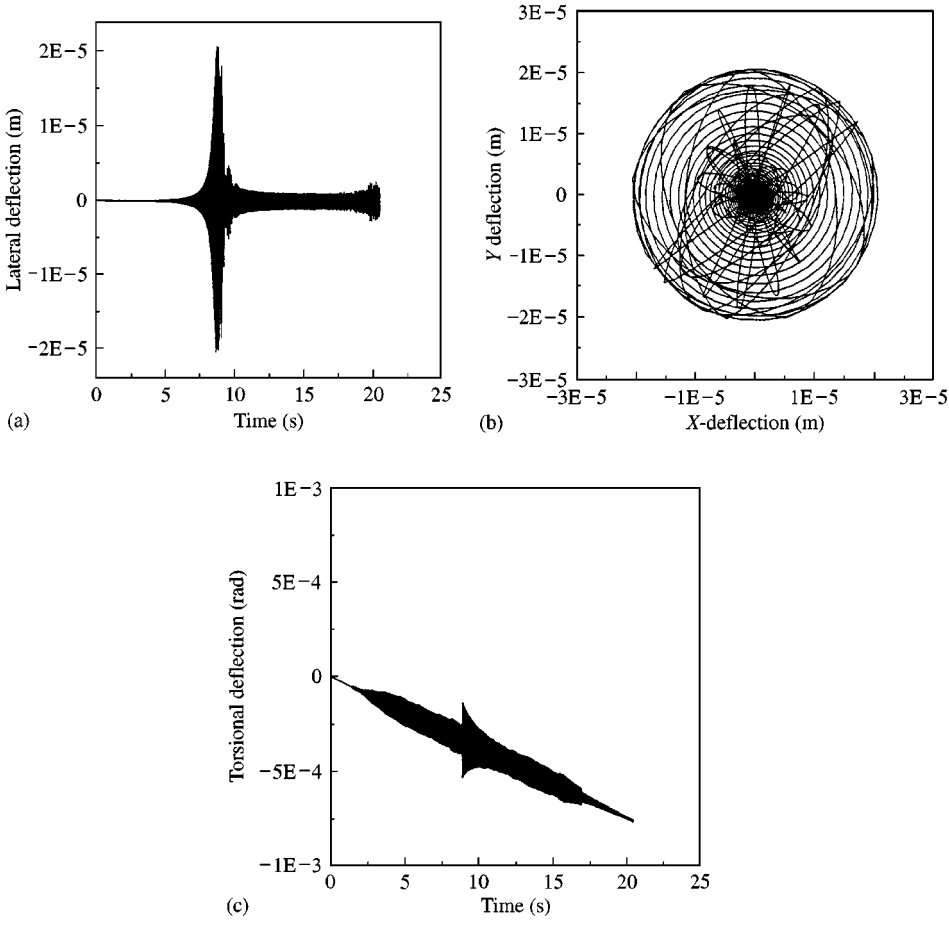

Figure 11. Rotor system response using the torsional–lateral-rotor model with $\omega_T \gg \omega_L$, non-zero cross-coupling bearing coefficients and under rubbing condition; (a) vertical deflection, (b) orbit, and (c) torsional deflection.

ACKNOWLEDGMENTS

The author acknowledges the support of King Fahd University of Petroleum and Minerals, Dhahran, Saudi Arabia.

REFERENCES

1. R. F. Beatty 1985 *Journal of Vibration, Acoustics, Stress, and Reliability in Design* **107**, 151–160. Differentiating rotor response due to radial rubbing.
2. F. F. Ehrich 1988 *Journal of Vibration, Acoustics, Stress, and Reliability in Design* **110**, 9–16, High order sub-harmonic response of high speed rotors in bearing clearance.
3. A. Muszynska 1984 *IMechE* **C281**, Partial lateral rotor to stator rubs.
4. A. Muszynska 1989 *The Shock and Vibration Digest* **21**, 3–11. Rotor-to-stationary element rub-related vibration phenomenon in rotating machinery-literature survey.

5. S. K. Choi and S. T. Noah 1994 *Journal of Applied Mechanics* **61**, 131–138. Mode-locking and chaos in Jeffcott rotor with bearing clearances.
6. P. Goldman and A. Muszynska 1994 *Journal of Engineering for Gas Turbines and Power* **116**, 692–701. Chaotic behavior of rotor/stator systems with rubs.
7. F. Chu and Z. Zhang 1998 *Journal of Sound and Vibration* **210**, 1–18. Bifurcation and chaos in rub-impact Jeffcott rotor system.
8. L. T. Tam, A. J. Prezkwas, A. Muszynska, R. C. Hendricks, M. J. Braun and R. L. Mullen 1988 *Journal of Vibration, Acoustics, Stress, and Reliability in Design* **110**, 315–325. Numerical and analytical study of fluid dynamic forces in seals and bearings.
9. M. Lallane and G. Ferraris 1990 *Rotordynamics Prediction in Engineering*. New York: John Wiley and Sons.
10. B. O. Al-Bedoor 1999 *Journal of Applied Mechanics* Modeling the coupled torsional and lateral vibrations of unbalanced rotors (submitted).